

Magnetic Fields in Star-Forming Molecular Clouds. IV. Polarimetry of the Filamentary NGC 2068 Cloud in Orion B

Brenda C. Matthews¹ & Christine D. Wilson

McMaster University, 1280 Main Street West, Hamilton Ontario, Canada L8S 4M1

bmatthews@astron.berkeley.edu

wilson@physics.mcmaster.ca

ABSTRACT

We present submillimeter polarimetry at 850 μm toward the filamentary star-forming region associated with the reflection nebulosity NGC 2068 in Orion B. These data were obtained using the James Clerk Maxwell Telescope's SCUBA polarimeter. The polarization pattern observed is not consistent with that expected for a field geometry defined by a single mean field direction. There are three distinct distributions of polarization angle, which could represent regions of differing inclination and/or field geometry within the filamentary gas. In general, the polarization pattern does not correlate with the underlying total dust emission. The presence of varying inclinations against the plane of the sky is consistent with the comparison of the 850 μm continuum emission to the optical emission from the Palomar Optical Sky Survey, which shows that the western dust emission lies in the foreground of the optical nebula while the eastern dust emission originates in the background. Percentage polarizations are high, particularly toward the north-east region of the cloud. The mean polarization percentage in the region is 5.0% with a standard deviation of 3.1%. Depolarization toward high intensities is identified in all parts of the filament.

Subject headings: ISM: clouds, magnetic fields, molecules — ISM: individual (NGC 2068) — polarization — stars: formation — submillimeter

1. Introduction

The study of polarized emission from molecular clouds is of great interest since, at long wavelengths ($\lambda > 25 \mu\text{m}$), it effectively traces the orientation on magnetic fields local to star-forming regions (Hildebrand 1988). Magnetic fields have been shown to be energetically comparable to gravity and kinetic motions within molecular clouds (Myers & Goodman 1988; Crutcher et al. 1999; Basu 2000) and are theorized to provide vital support to clouds, preventing global collapse (Mouschovias 1987; McKee et al. 1993, and references therein). Such support is necessary to explain the low star-forming efficiencies observed

in molecular clouds, including Orion B, where the efficiency is $\sim 1\%$ (Carpenter 2000).

The Orion B cloud, at a distance of ~ 415 pc (Anthony-Twarog 1982), is the closest giant molecular cloud. Within it, star formation is concentrated into five distinct regions: NGC 2071, NGC 2068, LBS 23 (HH 24), NGC 2024 and NGC 2023, as determined from unbiased surveys for young stellar objects (Lada et al. 1991a) and dense CS gas (Lada et al. 1991b). Large scale 850 μm dust emission from these regions has been mapped by Mitchell et al. (2001) and Motte et al. (2001). Maps of the polarized emission from NGC 2071, LBS 23, and NGC 2024 have already appeared in the literature (see Matthews et al. (2001a, hereafter Paper III)). In order to compare field geometries across Orion B, we have now mapped the polarized emission from NGC 2068.

¹Current Address: Department of Astronomy, 601 Campbell Hall, University of California Berkeley, Berkeley, CA 94720-3411

The submillimeter emission from NGC 2068 lies south of the reflection nebula (see Figure 1) which is seen optically and contains an infrared cluster (Lada et al. 1991a). The overall structure of the dust emission is that of a “clumpy filament” in which 18 distinct compact sources are identified. Most of the submillimeter sources fall outside the boundary of the cluster identified in CS by Lada et al. (1991b). Star formation is ongoing in this region, as evidenced by detections of bipolar outflows by Mitchell et al. (2001) around OriBN 51, from which evidence of outflow previously existed (Edwards & Snell 1984; Gibb & Little 2000), and also around OriBN 35 and OriBN 36 peaks (see their Fig. 1c or Figure 2 below), although the sources of these outflows are ambiguous due to the close proximity of OriBN 33 and OriBN 37 to the positions of high velocity gas. OriBN 39 has a 2MASS infrared source associated with it, and thus should be a source of outflow. Evidence for redshifted gas near OriBN 47 also suggests some outflow from this source.

There are no prior observations of polarized emission from the NGC 2068 dust emitting region. However, Mannion & Scarrott (1984) measured linear polarization from scattering against the reflection nebula north of the molecular condensations. Based on the centrosymmetric pattern observed, Mannion & Scarrott (1984) ruled out the presence of aligned grains within the reflection nebula. They infer the presence of a foreground assembly of grains illuminated from behind solely by the star HD 38563N. The position of this star is $\sim 5'$ north-east of the dust emission on which we report in this work, coincident with the near-IR cluster observed by Lada et al. (1991a).

Polarization data probe only two directions of the magnetic field geometry – those on the plane of the sky. Additionally, they provide no information about the strength of the magnetic field. Where field geometries are simple and the direction of the magnetic field does not vary through the cloud depth, the polarized emission detected is perpendicular to the mean magnetic field and the latter can be inferred simply by rotating the polarization vectors by 90° . If the field has a more complex, non-uniform geometry, then interpretation becomes more difficult. In such cases, it is best to compare directly the polarization maps with polarization patterns predicted from a phys-

ical model of a magnetized cloud. It is important to recognize that the polarizations measured are vector sums along a particular line of sight through the cloud observed, weighted by column density. Fiege & Pudritz (2000a) present a model for a filamentary cloud in which a helical magnetic field threads the filament and plays an important role in determining the radial density structure. This model predicts an r^{-2} density profile, which has been observed in several clouds, including the Integral-shaped Filament (Johnstone & Bally 1999) and several clouds in Cygnus (Lada, Alves & Lada 1999; Alves, Lada & Lada 1999). The helical field geometry also predicts depolarization toward the axis of a filament due to cancellation effects on either side of the axis. Fiege & Pudritz (2000b) present predicted polarization patterns for cases in which the field is either poloidally or toroidally dominated as well as for various filament inclinations. Qualitative extensions to these models have been shown to reproduce observed polarization patterns in the filamentary clouds OMC-3 (Matthews et al. 2001b, hereafter Paper II) and NGC 2024 (see Paper III). The filamentary structure of NGC 2068 is therefore of particular interest as a further test of axially symmetric magnetic field geometries.

This paper is the fourth in a series which seeks to compare the polarization patterns (and inferred magnetic field geometries) in different star-forming regions. The observations and data reduction techniques are described in §2. The polarization data are presented and analyzed in §3. The implications of these data for the local magnetic field geometry and that of Orion B as a whole are discussed in § 4, and § 5 summarizes our results.

2. Observations and Data Reduction

Using the UK/Japan polarimeter with the SCUBA (Submillimeter Common User Bolometer Array) detector at the James Clerk Maxwell Telescope² (JCMT), we have mapped polarized thermal emission from dust at $850 \mu\text{m}$ toward a filamentary dust cloud associated with the star-

²The JCMT is operated by the Joint Astronomy Centre on behalf of the Particle Physics and Astronomy Research Council of the UK, the Netherlands Organization for Scientific Research, and the National Research Council of Canada.

forming region NGC 2068. The observations were taken from 11 to 16 October 1999, and additional data were added on 18 February 2000. The polarizer and general reduction techniques are described in Greaves et al. (2001) and Greaves et al. (2000). More information on data reduction and systematic errors can be found in Paper II.

Six different SCUBA fields were required to map the entire NGC 2068 filament. Initially, four fields were used, but then the number of fields was increased and the positions shifted; hence 10 independent field centers were used. The field centers and other observing parameters are summarized in Table 1. The data were obtained using a 16 point jiggle-map mode, in which the telescope is “jiggled” in order to completely sample the SCUBA field. Chopping to a reference position was done to remove sky effects. The maximum chop throw possible is $180''$. We typically used $150''$ to ensure we were not chopping onto polarized emission. The extinction of the atmosphere, τ (225 GHz), ranged from 0.03 to 0.09 over the observations, but $> 85\%$ were taken when $\tau(225 \text{ GHz})$ was 0.06 or 0.07.

We have reduced the data using the Starlink software package POLPACK, designed to include polarization data obtained with bolometric arrays. The data have been corrected for an error in the SCUBA computer’s clock which placed incorrect LST times in the data headers from July 1999 to May 2000. This error did not affect the telescope’s acquisition or tracking but affects data reduction since the elevation and sky rotation are calculated from the LST times in the data files. The evolution of the magnitude of this error over time has been tracked and can therefore be corrected retroactively by adjusting the times in the headers (see the JCMT website for details). The error in timing after this adjustment is ± 10 s.

After extinction correction, noisy bolometers were identified and removed from the data sets. The data were sky subtracted using bolometers with mean values close to zero, but not those which were significantly negative. (The area mapped by each bolometer in a single jiggle map can be identified with reasonable accuracy, since little sky rotation occurs during the 16-point jiggle. Hence, by examining the flux levels of pixels within a bolometer, those in which a majority of adjacent pixels are negative were considered significantly negative and not used. Those for

which negative and positive values seem equally distributed can be considered to contain zero flux and be used for sky subtraction.) At $850 \mu\text{m}$, the sky is highly variable on timescales of seconds. This variability must be measured and removed from the data. Chopping removes the effects of slow sky variability; however, fast variations remain in the data, which require sky subtraction using array bolometers devoid of significant flux. We used between one and three bolometers to determine the sky variability, using the existing scan maps of total intensity at $850 \mu\text{m}$ (Mitchell et al. 2001) to help select empty bolometers. The methods of sky subtraction are discussed in detail in Jenness, Lightfoot & Holland (1998). As part of our analyses of other regions, we determined that sky subtraction can be done effectively with a single bolometer (see Paper II) and that the POLPACK reduction process is extremely robust with respect to the selection of sky bolometers (see Paper III). We have not added the mean flux removed by sky subtraction back into the NGC 2068 maps, since the flux in the sky positions was sufficiently close to zero (as determined from the large scale intensity map of Mitchell et al. (2001)).

Once the instrumental polarizations (IPs) were removed from each bolometer, all the data sets were combined to produce a final map in three Stokes’ parameters, I , Q and U , where I is the total, unpolarized intensity and Q and U are two orthogonal components of linearly polarized light. These three Stokes’ parameters were then combined to yield the polarization percentage, p , and polarization position angle, θ , in the map according to the relations:

$$p = \frac{\sqrt{Q^2 + U^2}}{I}; \quad \theta = \frac{1}{2} \arctan(U/Q). \quad (1)$$

The uncertainties in each of these quantities are given by:

$$dp = p^{-1} \sqrt{[dQ^2 + dU^2]}; \quad d\theta = 28.6^\circ / \sigma_p \quad (2)$$

where σ_p is the signal-to-noise in p , or p/dp .

A bias exists which tends to increase the p value, even when Q and U are consistent with $p = 0$, because p is forced to be positive. The polarization percentages were debiased according to the expression:

$$p_{ab} = \sqrt{p^2 - dp^2}. \quad (3)$$

Future references to polarization percentage, or p , refer to the debiased value.

In order to improve the σ_p , and hence $d\theta$, the data were binned to $15''$ sampling. This rebinning improves σ_p by a factor of five over the unbinned $3''$ sampled data. Good polarization vectors were selected to have $\sigma_p > 3$ (which implies $d\theta < 10^\circ$), $dp < 1\%$, $p > 1\%$ and be coincident with positions where the total unpolarized $850 \mu\text{m}$ flux exceeds 20% of the faintest of the six compact peaks, OriBN 35. The filtering of polarizations less than 1% accounts for the uncertainties in the IP values, as well as for any contamination due to sidelobe polarization, as discussed in Greaves et al. (2001). Sidelobe contamination refers to a polarized signal measured within the main beam due to a source within a sidelobe. If there is enough polarized flux ($p \times I$) from a source in a sidelobe position, a signal can be produced in the main beam despite the fact that the power in the JCMT sidelobes at $850 \mu\text{m}$ is typically $\leq 1\%$ that of the main beam. Greaves et al. (2001) derive the minimum believable polarization percentage, p_{crit} , based on: the ratio of power in the sidelobe to the main beam, P_{sl}/P_{mb} ; the ratio of unpolarized, total flux of the source in the sidelobe to that in the main beam, F_{sl}/F ; and the IP estimate at the sidelobe, p_{sl} :

$$p_{crit} \geq 2 \times p_{sl} \left(\frac{P_{sl}}{P_{mb}} \right) \left(\frac{F_{sl}}{F} \right). \quad (4)$$

We can estimate the extreme value of p_{crit} for the entire NGC 2068 region by calculating the worst case scenario. This occurs for the field centered at $\alpha(\text{J2000}) = 05^{\text{h}}46^{\text{m}}31^{\text{s}}.2$ and $\delta(\text{J2000}) = -00^\circ00'25''.5$, in which the brightest source in our map, OriBN 51, was approximately $54''$ from the center of the array. The beam responses and IP values are obtained from maps of unpolarized planets. Using polarization maps of Saturn from 14 October 1999, 16 October 1999 and 18 February 2000, the ratios of power in the sidelobe versus main beam are deduced to be 0.009, 0.01, and 0.004 respectively. The corresponding mean IP values at this sidelobe position are 4.5%, 4.7%, and 4.3%. The ratio of the flux of Ori BN 51 to the center of the field is ~ 7 . Hence, using equation (4), the p_{crit} values are determined to be 0.57%, 0.66%, and 0.24%. Thus, by selecting only values of $p > 1\%$, the polarizations cannot be attributable to sidelobe contamination.

3. NGC 2068 Polarization Data

Figure 2 shows the polarization data toward the NGC 2068 filamentary cloud. These data are displayed over a portion of the Mitchell et al. (2001) map of Orion B North. The polarization data are binned to $15''$, slightly greater than the $14''$ beamwidth of the JCMT at $850 \mu\text{m}$. Thus, each vector can be treated as an independent measurement of the local polarization at $850 \mu\text{m}$. The data are presented in tabular form in Appendix A. By eye, one can readily discern that three different populations of position angles exist within Figure 2. Separation of the data into three regions based on boundaries in RA can generally separate these populations. Figure 3 shows the distributions in position angle over the whole map, and for each of the three subsections. Region 1 encompasses the eastern part of the map, including all vectors east of the J2000 position of $05^{\text{h}}46^{\text{m}}39^{\text{s}}.8$. Region 2 is west of Region 1, extending to RA $05^{\text{h}}46^{\text{m}}33^{\text{s}}.8$ (J2000). Region 3 covers the western section of the map, including all vectors west of $05^{\text{h}}46^{\text{m}}33^{\text{s}}.8$ (J2000).

NGC 2068 contains six compact dust condensations (Mitchell et al. 2001), as well as a dozen more amorphous, fainter condensations. In the OMC-3 filament of Orion A, the polarization pattern was no different in the presence of embedded cores than elsewhere along the filament (Paper II). However, in Figure 2, polarization vectors near cores are smaller and more variable in direction, particularly near the cores OriBN 35, 47 and especially 51. In the latter case, no polarization is detected toward the core. Toward each of these cores, there is evidence of outflow; they are not pre-protostellar in nature. We note however that across the outflow source OriBN 39 and the compact core OriBN 38, the polarization vectors are consistent with the patterns surrounding the cores. The effect of the cores on the polarization pattern indicates that the filament is not dominating the polarized emission as was the case in OMC-3 in Orion A (see Matthews & Wilson (2000) and Paper II).

3.1. Polarization Position Angle and Filament Orientation

In Region 1, the mean polarization position angle is 109° east of north, which is equivalent to

-71° in linear polarization (since vectors offset by 180° are indistinguishable). The amorphous cores near the north-east have the highest polarizations, and the vector orientations there are roughly perpendicular to the projected filamentary axis, aligned in a roughly north-east to south-west orientation. Interestingly, the vectors along the three cores OriBN 34, 35 and 39 align well with those to the north-east, but now appear to lie parallel to the string of three cores. In Region 2, which includes the cores OriBN 37, 38 and part of 36, the vectors also follow the string of cores. Finally, in Region 3, which includes all cores west of OriBN 42, the polarization vectors are distributed about a mean of 74° , although the projected filament direction varies considerably. The vectors thus tend to follow the filament near OriBN 42 to 48, and then lie perpendicular to the filamentary dust emission along the whole eastern edge. Overall, there is no strong correlation between the filament orientation and the vector position angles.

Table 2 summarizes the statistics of the three data subsets plus the whole data set for the NGC 2068 region, as well as the results of single Gaussian fits to each of the position angle distributions shown in Figure 3. The mean position angle is denoted μ , while the width of the distribution is $w(\theta)$. The reduced chi-squared value is also listed and in each case is < 1 . The fit to Region 3 gives a mean of 66° with a width of 18° . Region 2 gives a mean of 93° with a width of 16° , and Region 1 yields a mean of 123° and width of 24° . The results of the fits are consistent with the statistical mean and standard deviation in the position angles.

3.2. Polarization Percentage

The results of a basic statistical analysis of the polarization percentage distributions in the NGC 2068 cloud and its subset of three regions are reported in Table 2. The mean polarization percentage in the whole filamentary cloud is 5.0% with a standard deviation of 3.1%. Similar values are found for each separate region within NGC 2068. No systematic variation in polarization percentage is obvious from examination of Table 2. Interestingly, Region 2 has the highest median value of p , and it is the only region where the median exceeds the mean, which indicates that in this region, po-

larization is high. The mean is not biased by only a few vectors of particularly high polarization percentage.

One of the most interesting properties of dust emission polarimetry has been the measurement of declining polarization percentage with increasing unpolarized intensity. Figure 4 shows this same trend in the NGC 2068 region and its subregions that has been observed in other regions. Over the entire data set, the variation of p with total intensity follows a power law of the form: $p = A \times I^\gamma$, where $\gamma = -0.81 \pm 0.04$ and $A = (1.6 \pm 0.4) \times 10^{-2}$. No systematic variation in polarization percentage between regions is evident from examination of Figure 4. We do note, however, that the effect is strongest in Region 3. In Region 1, the vectors surrounding the cores OriBN 31 and 32 are shown as filled triangles, while the rest of the region's vectors are plotted as open triangles. It is clear that the highest polarizations are observed at the extreme north-east of the NGC 2068 region.

As discussed in Paper II, a depolarization effect can be produced systematically by chopping the telescope during observing. However, based on that analysis, the steep profiles shown in Figure 4 could not be explained by this effect unless there were *significant* polarized flux in the chop position. For example, if the reference, or chop, position had 25% of the peak flux in the source field and was polarized to twice the degree of the source field, then a slope of -0.88 could be produced on a $\log p$ versus $\log I$ plot *in regions of low total intensity*. Even under this extreme scenario, in regions of high flux, we would not expect such a sharp decline in polarization percentage with intensity. We thus conclude that the depolarization effect in this region is not produced by systematic effects of chopping.

4. Discussion

4.1. Polarization Percentage in Orion B

Figure 5 shows the distributions of polarization percentage in the regions of Orion B observed with the SCUBA polarimeter. These distributions have been normalized to the total number of vectors measured in each region, and the counts expressed as a fraction of the total. The error bars represent the \sqrt{N} statistical uncertainty in the number of counts, also normalized to the total in each map.

The distribution for NGC 2068 is comparable to those measured in the other star-forming regions of Orion B North – NGC 2071 and LBS23N – and with measurements toward the OMC-3 filament in Orion A (Paper II). The NGC 2024 region is dominated by low percentage polarizations, with the majority between 1-2%. This result could imply NGC 2024 has weaker magnetic fields, poorer grain rotation or alignment, a different grain composition, or some combination of these factors. The fact that NGC 2071, NGC 2068 and LBS 23N show distributions which are reasonably flat from 1-6% could indicate similar grain properties, field strengths, and degrees of grain alignment, but this cannot be proven with these data. The densities toward the NGC 2024 cores have been estimated to be abnormally high (10^8 cm^{-3} Mezger et al. (1988)), but Schulz et al. (1991) suggest the values are more typical of cores (10^6 cm^{-3}). Polarization data at other wavelengths (such as $350 \mu\text{m}$) could help constrain the dust properties according to models (see Hildebrand et al. (2000) and references therein), and observations of dense molecular tracers like OH for Zeeman splitting could provide more detailed information about the field geometries in these four regions.

Toward all four regions of Orion B observed in polarized emission, the depolarization effect is detected (see Fig. 5 of Paper III and Figure 4). Paper III shows that NGC 2024 exhibits a similar depolarization signature to the northern core NGC 2071. However, LBS 23N has a significantly steeper slope of -0.95 , which is more consistent with that of Region 3 in our data set. This trend has been observed in many other regions as well, including massive cores such as OMC-1 (Schleuning et al. 1997) and protostellar and starless cores (Girart et al. 1999; Ward-Thompson et al. 2000).

4.2. Evidence for Varying Inclinations in NGC 2068

The filamentary dust emission of NGC 2068 likely arises from dust at different depths in the Orion B cloud. The comparison between the Palomar Observatory Sky Survey optical data and the dust emission has been made by Mitchell et al. (2001). We produce a similar image in Figure 1, which shows that while the western dust emission lines up well with the optically dark dust lane, the eastern dust emission has no correspond-

ing dark lane. (North of the H II region lies another dust condensation not yet observed with the polarimeter.) Hence, it is likely that the dust emission may lie on the outer edge of the reflection nebula with the western material in the foreground and the eastern material behind. Thus, it is clear that this filament does not lie in the plane of the sky, and that the inclination on the sky is likely variable.

An obvious question is whether or not all the dust emission arises from material which is spatially related. It is noteworthy that the core OriBN 34 does not appear to line up well with the filamentary material of Figure 2. In fact, our comparison of the optical and dust emission shows that the location of OriBN 34 is optically dark. This could be a coincidence, or OriBN 34 could be closer than the dust emission appearing next to it on the SCUBA image. OriBN 39 also appears dark and could be in the foreground. Mitchell et al. (2001) present $^{13}\text{CO } J = 2 - 1$ toward NGC 2068 and a partial map of the north-eastern region in $\text{C}^{18}\text{O } J = 2 - 1$ (see their Figs. 6 and 7). The ^{13}CO contours are closely correlated to the $850 \mu\text{m}$ dust emission. The same is true for the C^{18}O emission where data exist. These maps are integrated over velocity ranges from $5 \text{ km s}^{-1} < v_{LSR} < 15 \text{ km s}^{-1}$ and $7 \text{ km s}^{-1} < v_{LSR} < 13 \text{ km s}^{-1}$, respectively. Thus, the emission is confined to the Orion B cloud. The fact that OriBN 34 and 39 show similar polarization position angles as the eastern area but may be in the foreground would argue against these regions being completely spatially distinct (unless the cores are not contributing as much polarized emission as the background diffuse material. If the material is spatially separated, then the similar orientations of the polarization position angles could suggest that the field, if not defined by a single mean field direction, could be organized on spatial scales at least as large as the separation between them.

The $2.4 \mu\text{m}$ emission from the NGC 2068 reflection nebula spans approximately $6'$ in spatial extent (Sellgren 1984). This is consistent with the physical size of the nebula in optical emission as shown in Figure 1, and at a distance of 415 pc corresponds to 0.7 pc . If the nebula is as deep as it is wide, then the source of dust emission at the north-east could be more than a parsec displaced spatially from the cores at the west (taking $7'$ as

an estimate of their separation in projection).

4.3. Field Geometry

4.3.1. A Single Mean Field Direction

The vectors of NGC 2068 do not support a single field orientation in NGC 2068. If one assumes that the magnetic field geometry throughout a cloud's depth is reasonably well defined by a mean field direction, then the direction of the field can be obtained by rotating emission polarization data by 90° . Doing this in the NGC 2068 polarization map will clearly not produce aligned vectors, any more than the polarization data themselves are aligned. Therefore, we can rule out a uniform, unidirectional field across all of NGC 2068. This was also the case in OMC-3 in Orion A (see Paper II); however, in that region, the filamentary axis was easy to define, and a strong correlation between the axis and polarization position angle was observed along 75% of the filament. The vectors of NGC 2068 do not show an obvious alignment of polarization position angle with the filament orientation.

We can compare the polarization position angles across those regions observed thus far in Orion B. In the three regions of Orion B North, no evidence for similar polarization orientations exists. Toward NGC 2071, the polarization vectors align generally with the prominent outflow from the IRS 1 source at a position angle of 40° east of north. Within the LBS 23N string of cores to the south of NGC 2068, the vectors are generally aligned north-south (position angle 0°) although the scatter in this faint region is considerable. Neither of these orientations is dominant in NGC 2068. Thus, there is no support for a mean field direction in NGC 2068 or across the three star-forming regions of Orion B North.

The one region observed in Orion B South is NGC 2024, and the polarization pattern from that region has been modeled as arising either from a helical field geometry or from the expansion of the ionization front due to the associated H II region in Paper III. The latter geometry is favored since it is most compatible with the total physics and geometry of NGC 2024. It is clear that the polarization patterns across these star-forming regions can be strongly correlated with the dust and gas structures of a particular region, and that each

region must be modeled separately.

4.3.2. More Complex Geometries

As discussed above, there is evidence that the dust arises from a connected gas structure. However, the spatial separation between the filament edges could be > 1 pc. The regions of different position angles could indicate regions of different field geometry or inclinations. We propose two model geometries which could potentially explain the variable position angles observed.

Since the cores are mainly aligned along a filamentary structure, a helical field geometry is appealing. It can explain the confinement of gas in the filament, the fragmentation to cores and the elongation of the asymmetric concentrations along the axis of the filament, which is certainly the case for OriBN 31, 32, 33, 41 and 49. Fiege & Pudritz (2000b) show possible polarization patterns for different helical field conditions (i.e. poloidally-dominated versus toroidally-dominated). These models are developed for straight filaments, and Fiege & Pudritz (2000b) find that for such filaments, the polarization vectors align either parallel or perpendicular to the projected filament axis regardless of the inclination of the filament. However, Paper II presents a model for a helical field threading a bent filament. In this case, the vectors may adopt any orientation relative to the filament due to the asymmetries in the filament. The relative alignment depends on the filament's inclination and rotation on the plane of the sky.

Thus, as inclination and angle in the plane of the sky vary, a helically-threaded filament should produce different polarization position angles relative to the projected filament orientation. For instance, if the polarization positions are aligned with the filament, a toroidally-dominated helical field could wrap the filament locally. Conversely, where the vectors appear perpendicular to the filament, a helical field would be poloidally-dominated, or the filament and field could be significantly bent. At the north-western edge near the cores OriBN 33 and 41, the vectors are neither parallel nor perpendicular to the filament. This could also indicate that the filament is bent along its length in this area. Modeling such a complex filamentary structure will be difficult, since more than one filament/field geometry can produce similar polarization patterns.

One additional test for the presence of a helical field geometry is the radial profile of the total, unpolarized emission. Using the $850\ \mu\text{m}$ map of Mitchell et al. (2001), a radial profile can be built up by taking several slices across the filament. We have attempted to confine the cuts to the regions between cores along NGC 2068. Figure 6 shows the profiles through several such slices, taken between the OriBN 44 and 48, between 32 and 39 and between 35 and 36. For the second cut, both sides of the profile were used; for the other two, one side of the slice was discarded due to the presence of extended emission from the filament near OriBN 47 (for the cut between OriBN 44 and 48) and extended emission from core OriBN 34 (for the cut between OriBN35 and 36). The fluxes have been normalized to the maximum through the cuts (respectively $0.07\ \text{Jy beam}^{-1}$, $0.32\ \text{Jy beam}^{-1}$, and $0.28\ \text{Jy beam}^{-1}$); this position is assumed to be the axis of the filament. The NGC 2068 filament is so narrow and faint, it is difficult to interpret the profiles. To guide the eye, we have drawn on Figure 6 lines corresponding to slopes of -0.5 and -1 . Near the axis, the flux falls off with a distribution consistent with a power law index of -0.5 . Toward lower fluxes, the index could be closer to -1 ; however, at these low flux levels, interpretation of the index becomes difficult. The flux profile of $r^{-0.5}$ corresponds to a density profile of $r^{-1.5}$ for an isothermal filament. The helical field geometry predicts a density profile with index -2 for an isothermal equation of state. For other equations of state (e.g. the logtrope, McLaughlin & Pudritz (1996)), a shallower range of density profiles can be generated. Unmagnetized, isothermal filaments predict much steeper profiles, with indices of -4 , which are clearly not consistent even with these poor profiles.

A second possible field geometry is suggested by the position of the molecular filament so near the periphery of the reflection nebula of NGC 2068. Paper III presents a model of the polarization data toward the NGC 2024 dense ridge of cores in which the field, compressed by the expansion of the NGC 2024 H II region, is then moulded around the dense ridge as the ionization front approaches the cores. This picture accounts for both the polarization pattern at $850\ \mu\text{m}$ and the measurements of the line-of-sight field direction and strength measured by Crutcher et al. (1999). The expansion of the

reflection nebula could produce a similar effect in NGC 2068, although the pattern produced is much more complex. In NGC 2024, the ridge is entirely located on the far-side of the H II region, whereas in NGC 2068 the comparison of optical and $850\ \mu\text{m}$ dust emission in Figure 1 indicates that the dust emission arises from both the near and far-side of the nebula.

A recent publication on the formation of quiescent cores through turbulent flows (Padoan et al. 2001) provides a third possible interpretation of the polarization pattern. This work discusses the potential formation of cores due to the presence of super-sonic turbulent flows within molecular clouds. In this model, cores form by accretion along filamentary structures, with the brightest cores forming at the loci of intersecting shocks. The core OriBN 47 lies at the intersection of three filamentary segments. As predicted by Padoan et al. (2001), this core exhibits depolarization, although at the distance of Orion B, it is difficult to achieve a good sampling of polarization vectors across this core. Thus, we do not see the large changes in position angle predicted near cores (see their Fig. 3) and routinely observed in Bok globules and starless cores in closer regions of star formation (e.g. see Ward-Thompson et al. (2000)). However, the polarization pattern along the larger scale filamentary structure is well sampled in our map. In the turbulent flows model, the polarization vectors along the filamentary structures are seen to align well with the filaments' axes. In NGC 2068, only the filament segment east of OriBN 48 exhibits this behavior. The segments to the north-west and south-west show vectors oriented roughly perpendicular to the filamentary structure, which does not agree well with the turbulent flows picture. A simulation of turbulent flows along filaments of higher density may agree better with our observations in NGC 2068. If a threshold in extinction exists beyond which grains are not effectively aligned (Padoan et al. 2001), then denser turbulent flows could exhibit less correlation between the filamentary axis and the inferred polarization.

5. Summary

We have detected polarized emission from aligned dust grains at $850\ \mu\text{m}$ with the SCUBA

polarimeter. These data reveal strong degrees of polarization (up to 17%) toward the NGC 2068 region, with higher polarization percentages detected toward regions of fainter total intensity. This depolarization effect has been observed in most regions of polarized emission. Significant depolarization has been detected toward several compact cores along the filament. Within the cores of LBS 23N and some cores along the NGC 2024 dense ridge, significant depolarization was also measured (see Paper III) We note that this was not the case in the OMC-3 filament of Orion A, where the polarization patterns behaved consistently in the presence or absence of embedded cores (see Paper I and Paper II). This was attributed to the fact that filamentary dust dominated the polarization pattern in Orion A, but that this is not the case in Orion B.

The polarization pattern is inconsistent with that expected for a uniform field geometry, for which vectors should be aligned with one another across the entire region. The polarization position angles are roughly organized into three distinct distributions which do not align with the orientations of the filamentary total intensity emission. This is also different than the pattern observed in the OMC-3 part of the Integral-shaped Filament in Paper II where the vectors aligned with the filament orientation along 75% of the filament's length. Taken in comparison with the polarization data for three other star-forming regions in Orion B (Paper III), there is also no evidence for a single field orientation across the Orion B cloud as a whole.

Comparison of optical and 850 μm dust emission establishes that the dust filament is not lying in the plane of the sky, but must be twisted such that its western edge is in the foreground of the optical reflection nebula, while the eastern edge lies behind. These changes in inclination can help explain the polarization pattern observed. Paper II shows that a bent filament threaded by a helical field geometry can produce polarization vectors offset from the filament orientations by varying degrees. Material lying on the edge of an expanding reflection nebula could also exhibit different magnetic field orientations at different locations depending on how effectively the field has been compressed by the expansion. The complexity of this filamentary structure will make modeling dif-

ficult, since there may be many degenerate choices of filament/field configurations which can produce the observed polarization pattern.

These are the first observations of polarized emission toward this filament. The strength of the polarization percentages detected suggests that polarized emission should be detectable at other wavelengths. For instance, observations at 350 μm with the Hertz polarimeter would provide some information on the polarization spectrum for this region. This could lead to constraints on the grain population along the filament. Additionally, Zeeman data on B_{los} field would provide significant constraint to the three-dimensional field structure.

The authors thank the members of the Canadian Consortium on Star Formation for the 850 μm scan map of the Orion B North cloud. Thanks to J. Greaves, T. Jenness, and G. Moriarty-Schieven at the JCMT for assistance during and after observing. The research of BCM and CDW has been supported through grants from the Natural Sciences and Engineering Research Council of Canada. BCM acknowledges funding from Ontario Graduate Scholarships during the period of this research.

REFERENCES

- Alves, J., Lada, C.J., & Lada, E.A. 1999, *ApJ*, 515, 265
- Anthony-Twarog, B. J. 1982, *AJ*, 87, 1213
- Basu, S. 2000, *ApJ*, 540, 103
- Carpenter, J. M. 2000, *AJ*, 120, 3139
- Crutcher, R. M., 1999, *ApJ*, 520, 706
- Crutcher, R.M., Roberts, D.A., Troland, T.H., & Goss, W.M. 1999, *ApJ*, 515, 275
- Edwards, S. & Snell, R.L. 1984, *ApJ*, 281, 237
- Fiege, J.D., & Pudritz, R.E. 2000a, *MNRAS*, 311, 85
- Fiege, J.D., & Pudritz, R.E. 2000b, *ApJ*, 544, 830
- Gibb, A.G., & Little, L.T. 2000, *MNRAS*, 313, 663
- Girart, J.M., Crutcher, R.M., & Rao, R. 1999, *ApJ*, 525, 109

- Greaves, J.S., Holland, W.S., Jenness, T., Moriarty-Schieven, G., Chrysostomou, A., Berry, D.S., Murray, A.G., Nartallo, R., Ade, P.A.R., Gannaway, F., Haynes, C.V., Tamura, M., Momose, M., & Morino, J.-I. 2001, MNRAS, submitted
- Greaves, J.S., Jenness, T., Chrysostomou, A.C., Holland, W.S., & Berry, D.S. 2000, in *Imaging at Radio through Submillimeter Wavelengths*, eds. J.G. Mangum & S.J.E. Radford, ASP-CS 217, 18
- Hildebrand, R.H. 1988, QJRAS, 29, 327
- Hildebrand, R. H., Davidson, J. A., Dotson, J. L., Novak, G., & Vaillancourt, J. E. 2000, PASP, 112, 1215
- Jenness, R., Lightfoot, J.F., & Holland, W.S. 1998, Proc. SPIE, 3357, 548
- Johnstone, D., & Bally, J. 1999, ApJ, 510, L49
- Lada, C.J., Alves, J., & Lada, E.A. 1999, ApJ, 512, 250
- Lada, E. A., Bally, J., & Stark, A. A. 1991a, ApJ, 368, 432
- Lada, E. A., DePoy, D. L., Evans, N. J., & Gatley, I. 1991b, ApJ, 371, 171
- Mannion, M.D., & Scarrott, S.M. 1984, MNRAS, 208, 905
- Matthews, B. C., & Wilson, C. D. 2000, ApJ, 531, 868 (Paper I)
- Matthews, B.C., Fiege, J.D., & Moriarty-Schieven, G. 2001a, submitted to ApJ(Paper III)
- Matthews, B.C., Wilson, C.D., & Fiege, J.D. 2001b, ApJ, 562, 400 (Paper II)
- McKee, C. F., Zweibel, E. G., & Goodman, A. A. 1993, in *Protostars and Planets III*, 327
- McLaughlin, D. E., & Pudritz, R. E. 1996, ApJ, 469, 194
- Mezger, P. G., Chini, R., Kreysa, E., Wink, J. W., & Salter, C. J. 1988, A&A, 191, 44
- Mitchell, G.F., Johnstone, D., Moriarty-Schieven, G., Fich, M., & Tothill, N.F.H. 2001, ApJ, 556, 215
- Motte, F., André, P., Ward-Thompson, D., & Bontemps, S. 2001, A&A, 372, 41
- Mouschovias, T. C. 1987, in *Physical Processes in Interstellar Clouds*, 453
- Myers, P.C., & Goodman, A.A. 1988, ApJ, 326, L27
- Padoan, P., Goodman, A.A., Draine, B., Juvela, M., Nordlund, Å., & Rönigvaldsson, Ö. 2001, ApJ, 559, 1005
- Schleuning, D.A., Dowell, C.D., Hildebrand, R.H., Platt, S.R., & Novak, G. 1997, PASP, 109, 307
- Schulz, A., Güsten, R., Zylka, R., & Serabyn, E. 1991, A&A, 246, 570
- Sellgren, K. 1984, ApJ, 277, 623
- Ward-Thompson, D., Kirk, J.M., Crutcher, R.M., Greaves, J.S., Holland, W.S., & André, P. 2000, ApJ, 537, 135

This 2-column preprint was prepared with the AAS L^AT_EX macros v5.0.

A. The Polarization Data

Table 3 contains the polarization data plotted in Figure 2. Positional offsets are given from the J2000 coordinates $\alpha = 05^{\text{h}}46^{\text{m}}33^{\text{s}}.8$ and $\delta = 00^{\circ}01'43''.0$ ($\alpha = 05^{\text{h}}44^{\text{m}}00^{\text{s}}.0$ and $\delta = 00^{\circ}00'00''.0$ in B1950). Vectors are binned to $15''$ sampling and all have $\sigma_p > 3$, $p > 1\%$, and an absolute uncertainty in polarization percentage, $dp < 1\%$. The total intensity at the vector position exceeds 20% of the faintest compact peak, OriBN 35. This minimizes the chances of systematic effects from chopping to a reference position, as discussed in Appendix A of Paper II.

TABLE 1
OBSERVING PARAMETERS FOR JIGGLE MAPPING

Pointing Center		Chop Position Angle	Number of
R.A. (J2000)	Dec. (J2000)	(east of north)	Times Observed
05 ^h 46 ^m 26 ^s .5	+00°00'21".9	40°	3
05 ^h 46 ^m 30 ^s .5	−00°01'48".4	90°	3
05 ^h 46 ^m 37 ^s .6	+00°00'33".1	155°	3
05 ^h 46 ^m 47 ^s .9	+00°01'00".3	155°	3
05 ^h 46 ^m 25 ^s .7	+00°00'34".9	40°	17
05 ^h 46 ^m 28 ^s .7	−00°01'55".3	90°	18
05 ^h 46 ^m 31 ^s .2	−00°00'25".5	165°	18
05 ^h 46 ^m 39 ^s .2	+00°00'48".9	155°	13
05 ^h 46 ^m 44 ^s .7	+00°00'33".5	155°	12
05 ^h 46 ^m 50 ^s .3	+00°01'23".1	155°	11

NOTE.—The chop throw used for all observations was 150", with the exception of the pointing centre $\alpha = 05^{\text{h}}46^{\text{m}}31^{\text{s}}.2$ and $\delta = -00^{\circ}00'25''.5$, for which the throw was 180".

TABLE 2
POLARIZATION PERCENTAGE AND POSITION ANGLE WITHIN NGC 2068

Region	# Vectors	Statistics				Gaussian Fits			
		$\langle p \rangle$ (%)	Median p (%)	$s(p)$ (%)	$\langle \theta \rangle$ (°)	$s(\theta)$ (°)	μ (°)	$w(\theta)$ (°)	χ_{red}^2
1	68	4.9	3.6	3.6	109.2	41	123	24	0.7
2	26	4.7	5.2	2.2	93.4	16	93	16	0.4
3	69	5.2	4.8	2.9	74.3	35	66	18	0.7
all	163	5.0	4.3	3.1	91.4	40	95	41	0.2

TABLE 3
NGC 2068 850 μM POLARIZATION DATA

Δ R.A. ($''$)	Δ DEC. ($''$)	p (%)	dp (%)	σ_p	θ ($^\circ$)	$d\theta$ ($^\circ$)
-36.0	-244.5	11.22	0.96	11.7	-69.3	2.5
-36.0	-229.5	1.65	0.28	5.8	-48.9	4.9
-51.0	-229.5	2.39	0.47	5.1	51.9	5.6
-6.0	-214.5	8.62	0.85	10.1	45.0	2.8
-51.0	-214.5	1.24	0.20	6.2	-76.1	4.6
-66.0	-214.5	5.17	0.59	8.7	-82.6	3.3
-21.0	-199.5	2.01	0.57	3.5	-50.8	8.1
-51.0	-199.5	1.96	0.31	6.2	75.4	4.6
-66.0	-199.5	3.40	0.44	7.8	43.8	3.7
-81.0	-199.5	6.16	0.65	9.5	66.8	3.0
-66.0	-184.5	6.91	0.41	16.9	71.1	1.7
-81.0	-184.5	4.46	0.45	10.0	-75.7	2.9
-96.0	-184.5	7.21	0.62	11.6	46.5	2.5
-66.0	-169.5	4.11	0.43	9.5	52.5	3.0
-81.0	-169.5	4.75	0.30	15.7	73.1	1.8
-96.0	-169.5	2.38	0.39	6.1	-84.2	4.7
-66.0	-154.5	6.16	0.46	13.5	64.6	2.1
-81.0	-154.5	2.65	0.27	9.9	74.3	2.9
-96.0	-154.5	5.59	0.37	15.2	74.7	1.9
-51.0	-139.5	4.26	0.52	8.2	80.0	3.5
-66.0	-139.5	3.10	0.29	10.5	68.3	2.7
-81.0	-139.5	3.86	0.25	15.2	51.7	1.9
-96.0	-139.5	2.28	0.33	7.0	4.1	4.1
-36.0	-124.5	6.03	0.43	14.0	74.2	2.0
-51.0	-124.5	5.70	0.32	17.6	84.0	1.6
-66.0	-124.5	3.22	0.23	14.1	77.2	2.0
-81.0	-124.5	2.86	0.15	19.6	68.1	1.5
-96.0	-124.5	2.06	0.19	10.9	58.6	2.6
-21.0	-109.5	8.99	0.46	19.5	49.5	1.5
-36.0	-109.5	6.78	0.59	11.4	63.6	2.5
-66.0	-109.5	5.12	0.42	12.2	59.9	2.4
-81.0	-109.5	1.12	0.15	7.7	27.8	3.7
-96.0	-109.5	3.22	0.22	14.5	81.6	2.0
-126.0	-109.5	4.21	0.62	6.8	-36.5	4.2
-141.0	-109.5	7.42	0.80	9.3	40.2	3.1
-6.0	-94.5	6.00	0.63	9.5	43.9	3.0
-21.0	-94.5	4.32	0.52	8.3	-4.2	3.5
-81.0	-94.5	12.43	0.63	19.7	48.2	1.5
-96.0	-94.5	14.80	0.56	26.5	69.9	1.1
-111.0	-94.5	11.26	0.74	15.3	56.0	1.9
-126.0	-94.5	2.80	0.39	7.2	61.0	4.0

TABLE 3—*Continued*

Δ R.A. (")	Δ DEC. (")	p (%)	dp (%)	σ_p	θ ($^\circ$)	$d\theta$ ($^\circ$)
-141.0	-94.5	4.12	0.34	12.3	-87.7	2.3
-156.0	-94.5	5.16	0.76	6.8	88.2	4.2
9.0	-79.5	3.66	0.69	5.3	-57.8	5.4
-6.0	-79.5	1.78	0.45	3.9	-77.3	7.3
-126.0	-79.5	4.33	0.49	8.9	61.8	3.2
-141.0	-79.5	1.18	0.35	3.4	-21.7	8.4
-156.0	-79.5	4.88	0.59	8.3	-56.1	3.5
24.0	-64.5	5.22	0.67	7.8	76.6	3.7
9.0	-64.5	3.30	0.45	7.4	44.5	3.9
-111.0	-64.5	6.96	0.71	9.8	47.9	2.9
-126.0	-64.5	4.77	0.33	14.3	88.1	2.0
-141.0	-64.5	5.11	0.28	18.1	75.4	1.6
-156.0	-64.5	7.09	0.48	14.9	77.9	1.9
-171.0	-64.5	7.00	0.91	7.7	68.8	3.7
234.0	-49.5	7.74	0.82	9.4	-14.0	3.0
219.0	-49.5	2.41	0.61	4.0	42.0	7.2
204.0	-49.5	1.42	0.30	4.8	-0.1	6.0
189.0	-49.5	1.72	0.38	4.6	73.5	6.3
174.0	-49.5	1.39	0.46	3.0	-42.5	9.5
159.0	-49.5	1.47	0.39	3.8	-65.7	7.6
129.0	-49.5	2.88	0.48	6.0	-82.6	4.8
114.0	-49.5	2.97	0.46	6.4	71.5	4.5
99.0	-49.5	4.06	0.46	8.9	70.8	3.2
84.0	-49.5	4.06	0.56	7.3	-85.0	3.9
69.0	-49.5	4.47	0.67	6.6	-71.8	4.3
54.0	-49.5	7.57	0.74	10.2	75.6	2.8
39.0	-49.5	7.18	0.62	11.5	81.4	2.5
24.0	-49.5	5.39	0.46	11.7	-82.3	2.4
9.0	-49.5	5.09	0.45	11.3	-67.5	2.5
-6.0	-49.5	3.51	0.71	4.9	67.4	5.8
-111.0	-49.5	6.93	0.62	11.2	-12.5	2.6
-141.0	-49.5	3.84	0.42	9.1	-87.1	3.1
-156.0	-49.5	10.14	0.70	14.4	-87.9	2.0
234.0	-34.5	3.63	0.49	7.4	2.4	3.9
219.0	-34.5	2.48	0.29	8.6	-16.0	3.3
204.0	-34.5	1.39	0.15	9.0	-26.4	3.2
189.0	-34.5	2.18	0.23	9.5	-52.6	3.0
174.0	-34.5	1.80	0.41	4.4	-45.6	6.5
159.0	-34.5	1.44	0.31	4.6	-53.0	6.2
144.0	-34.5	2.54	0.26	9.8	-56.1	2.9
129.0	-34.5	1.59	0.27	5.9	-55.9	4.9

TABLE 3—*Continued*

Δ R.A. (")	Δ DEC. (")	p (%)	dp (%)	σ_p	θ ($^\circ$)	$d\theta$ ($^\circ$)
114.0	-34.5	2.14	0.29	7.4	-72.6	3.9
99.0	-34.5	5.08	0.26	19.2	88.1	1.5
84.0	-34.5	1.43	0.31	4.7	55.2	6.2
69.0	-34.5	3.34	0.27	12.3	-72.6	2.3
54.0	-34.5	4.38	0.27	16.3	76.5	1.8
39.0	-34.5	5.37	0.32	16.9	81.8	1.7
24.0	-34.5	5.23	0.33	15.7	-89.6	1.8
9.0	-34.5	6.04	0.42	14.3	88.4	2.0
-6.0	-34.5	4.19	0.84	5.0	7.0	5.7
-126.0	-34.5	7.35	0.65	11.3	57.2	2.5
-141.0	-34.5	12.61	0.70	18.0	65.6	1.6
249.0	-19.5	4.22	0.86	4.9	-36.0	5.9
234.0	-19.5	5.38	0.57	9.4	6.0	3.0
219.0	-19.5	2.83	0.42	6.7	-19.0	4.3
204.0	-19.5	3.91	0.34	11.6	-52.7	2.5
189.0	-19.5	4.35	0.41	10.5	-56.9	2.7
174.0	-19.5	4.84	0.53	9.2	-60.0	3.1
159.0	-19.5	2.47	0.33	7.4	-74.4	3.9
144.0	-19.5	1.55	0.19	8.1	-67.2	3.5
129.0	-19.5	1.10	0.19	5.7	22.6	5.0
99.0	-19.5	3.64	0.24	15.1	-89.7	1.9
84.0	-19.5	2.84	0.31	9.2	-82.2	3.1
69.0	-19.5	1.70	0.33	5.2	-78.0	5.6
54.0	-19.5	1.94	0.34	5.8	77.4	5.0
39.0	-19.5	9.12	0.39	23.5	-83.3	1.2
24.0	-19.5	5.51	0.48	11.5	87.3	2.5
9.0	-19.5	9.28	0.96	9.7	90.0	3.0
-96.0	-19.5	5.40	0.52	10.4	55.9	2.7
-111.0	-19.5	6.52	0.64	10.3	37.8	2.8
264.0	-4.5	5.51	0.95	5.8	39.6	5.0
249.0	-4.5	4.84	0.54	8.9	31.3	3.2
234.0	-4.5	4.28	0.53	8.0	15.5	3.6
219.0	-4.5	2.82	0.43	6.6	-39.5	4.3
204.0	-4.5	2.89	0.37	7.7	-73.0	3.7
189.0	-4.5	3.55	0.53	6.7	-88.2	4.3
174.0	-4.5	3.93	0.67	5.9	-47.0	4.9
144.0	-4.5	1.53	0.29	5.2	11.4	5.5
114.0	-4.5	1.75	0.35	5.0	-19.3	5.7
99.0	-4.5	3.05	0.25	12.0	-88.2	2.4
84.0	-4.5	1.66	0.28	6.0	76.1	4.7
54.0	-4.5	5.60	0.82	6.8	8.5	4.2

TABLE 3—*Continued*

Δ R.A. (")	Δ DEC. (")	p (%)	dp (%)	σ_p	θ ($^\circ$)	$d\theta$ ($^\circ$)
39.0	-4.5	7.16	0.88	8.1	-26.0	3.5
-96.0	-4.5	2.51	0.35	7.2	51.9	4.0
-111.0	-4.5	4.12	0.40	10.3	27.6	2.8
249.0	10.5	2.21	0.62	3.6	42.6	8.0
234.0	10.5	2.74	0.37	7.4	-67.2	3.9
219.0	10.5	3.06	0.26	11.5	-77.8	2.5
204.0	10.5	5.40	0.36	15.1	-62.1	1.9
189.0	10.5	10.42	0.72	14.4	-69.2	2.0
174.0	10.5	7.38	0.80	9.2	-60.9	3.1
159.0	10.5	5.88	0.73	8.1	-46.7	3.5
144.0	10.5	5.63	0.64	8.8	-59.5	3.3
129.0	10.5	3.20	0.45	7.1	-26.9	4.1
114.0	10.5	3.38	0.40	8.4	-45.9	3.4
99.0	10.5	1.90	0.29	6.5	-37.4	4.4
84.0	10.5	1.95	0.26	7.4	-72.2	3.9
-81.0	10.5	5.90	0.66	9.0	81.3	3.2
-96.0	10.5	3.76	0.36	10.5	55.4	2.7
-111.0	10.5	3.60	0.53	6.8	13.4	4.2
249.0	25.5	13.06	0.96	13.6	-7.9	2.1
234.0	25.5	6.99	0.53	13.2	-51.4	2.2
219.0	25.5	6.16	0.31	20.1	-53.4	1.4
204.0	25.5	8.99	0.34	26.1	-65.6	1.1
189.0	25.5	17.07	0.70	24.5	-65.0	1.2
114.0	25.5	8.63	0.86	10.1	-33.3	2.8
99.0	25.5	2.83	0.56	5.0	-21.0	5.7
69.0	25.5	5.62	0.92	6.1	-53.3	4.7
-81.0	25.5	6.53	0.75	8.7	57.9	3.3
-96.0	25.5	2.93	0.52	5.6	64.0	5.1
-111.0	25.5	8.23	0.90	9.1	-31.6	3.1
234.0	40.5	8.20	0.77	10.6	-58.5	2.7
219.0	40.5	8.08	0.43	18.6	-64.5	1.5
204.0	40.5	15.63	0.51	30.5	-77.3	0.9
264.0	55.5	3.27	0.83	3.9	-88.3	7.3
249.0	55.5	6.25	0.58	10.8	-72.3	2.7
234.0	55.5	6.74	0.47	14.3	-49.5	2.0
219.0	55.5	6.48	0.54	12.1	-69.9	2.4
204.0	55.5	7.45	0.95	7.8	-84.8	3.7
249.0	70.5	6.72	0.73	9.2	-44.0	3.1
234.0	70.5	12.65	0.59	21.6	-59.1	1.3
219.0	70.5	15.56	0.93	16.7	-78.9	1.7

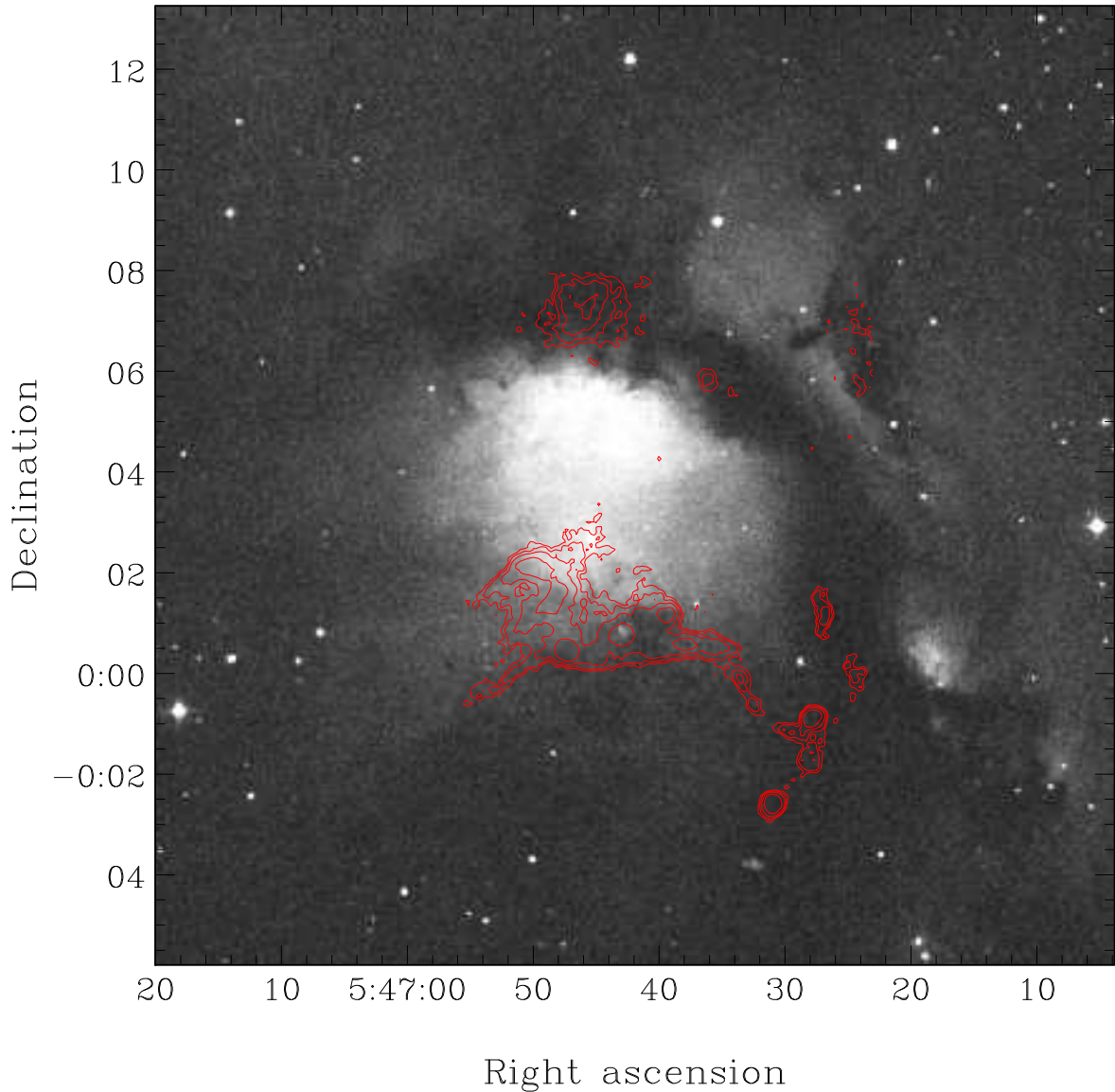


Fig. 1.— The optical and dust emission from NGC 2068. The optical image from the Palomar Sky Survey is presented, covering an area of $\sim 20' \times \sim 20'$. The NGC 2068 reflection nebula is central. The SCUBA total, unpolarized dust emission at $850 \mu\text{m}$ is shown in contours of 90, 93, 96 and 99 percentiles from Mitchell et al. (2001). The western edge of the dust emission appears to be coincident with the optical dust lane. At the east, however, the region of dust emission appears bright in the optical, and hence the dust must lie behind the nebula. A northern dust peak has not yet been observed with the polarimeter.

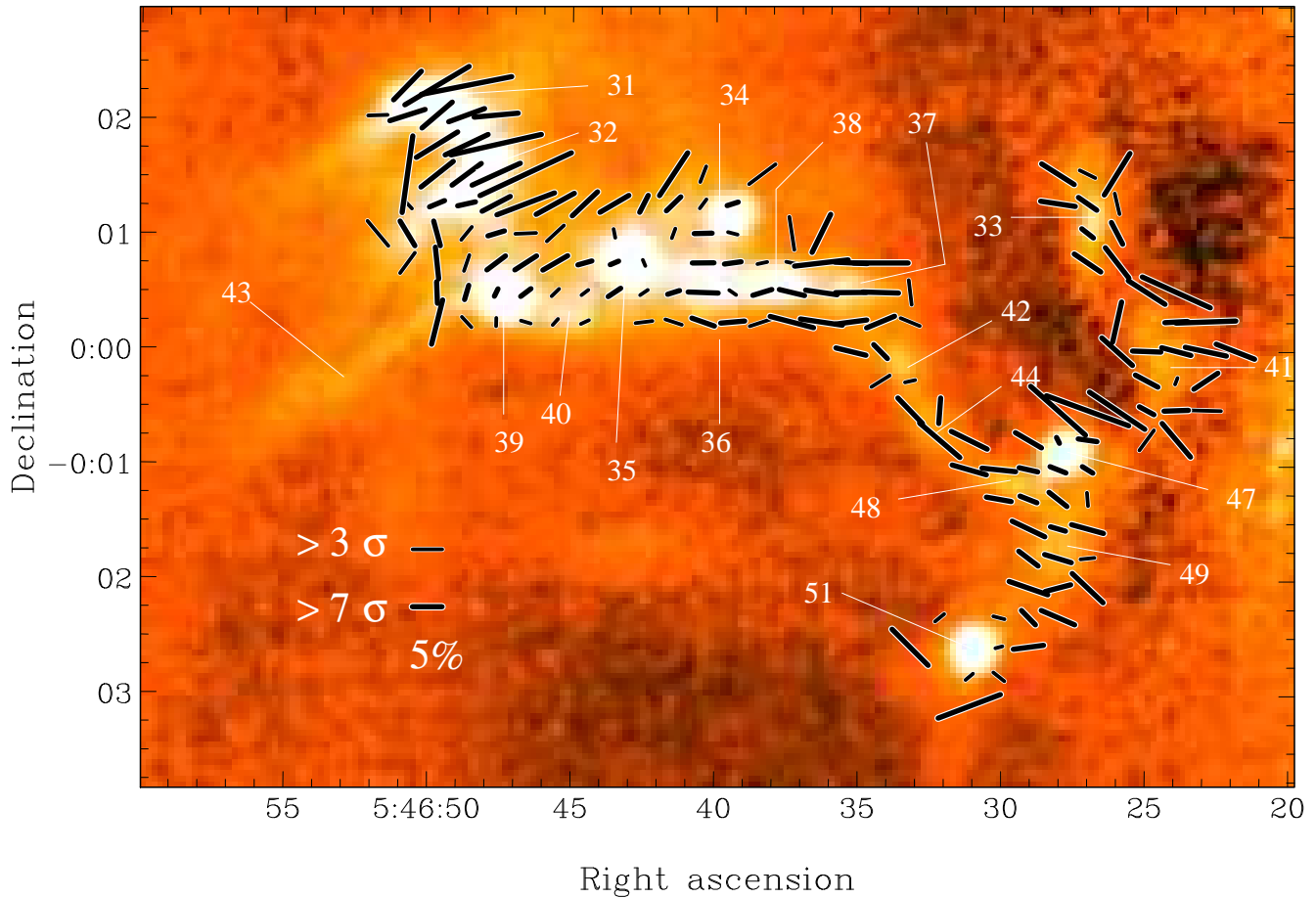


Fig. 2.— The $850 \mu\text{m}$ polarization pattern across NGC 2068. The colored greyscale is a more spatially extensive scan map provided by Mitchell et al. (2001). The greyscale range is -2σ to 3σ . Polarization data were sampled at $3''$ and have been binned to $15''$ ($>$ the JCMT beamwidth). All vectors plotted are coincident with location where the total, unpolarized intensity $> 20\%$ that of OriBN 35 (10% that of OriBN 51). The thin vectors have signal-to-noise $\sigma_p > 3$, while the thick vectors have $\sigma_p > 7$. The thin vectors are accurate in position angle to better than 10° , while the thicker vectors are accurate to better than 4° . The coordinates of the map are J2000.

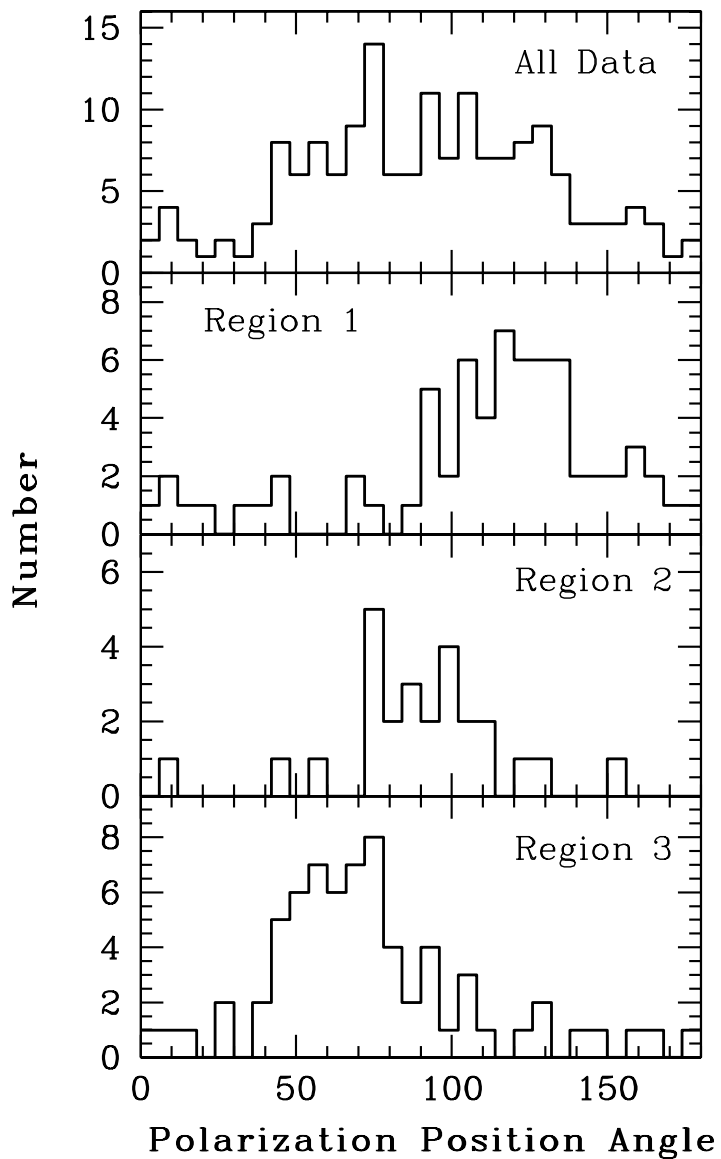


Fig. 3.— The distribution of polarization position angle in NGC 2068. The position angles of all vectors plotted on Figure 2 are presented in the top panel. The distribution of vectors has a mean of 91.4° and standard deviation about the mean of 40° . Additionally, the distribution of position angles in all three subsets of the data as defined in the text are shown.

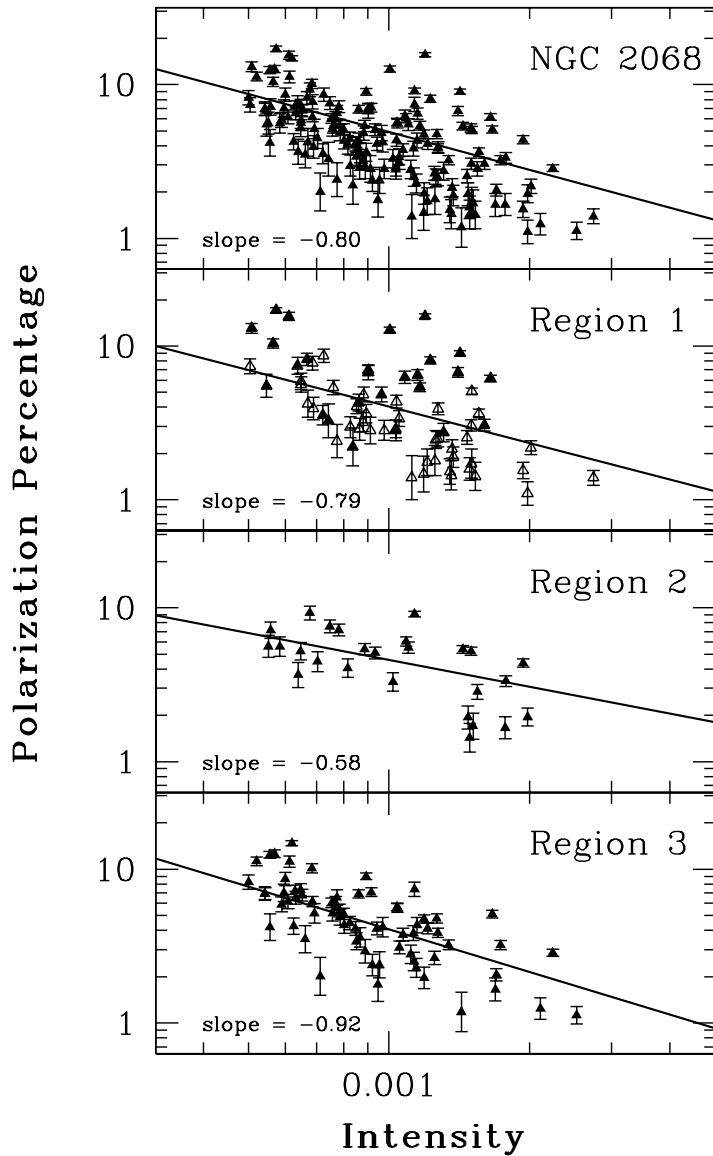


Fig. 4.— The depolarization effect in NGC 2068. We have plotted p versus I in log space and included fits to the corresponding p versus I profiles. The fits are to the power law: $p = A \times I^\gamma$, where γ is shown as the slope of the log-log plot. Plots are shown for each of the subregions discussed in the text. The Region 1 panel illustrates positions at the extreme north-east (near OriBN 31 and 32) as filled triangles, while the rest of the vectors in the area are plotted as open triangles. The strongest polarizations are located in the north-east area.

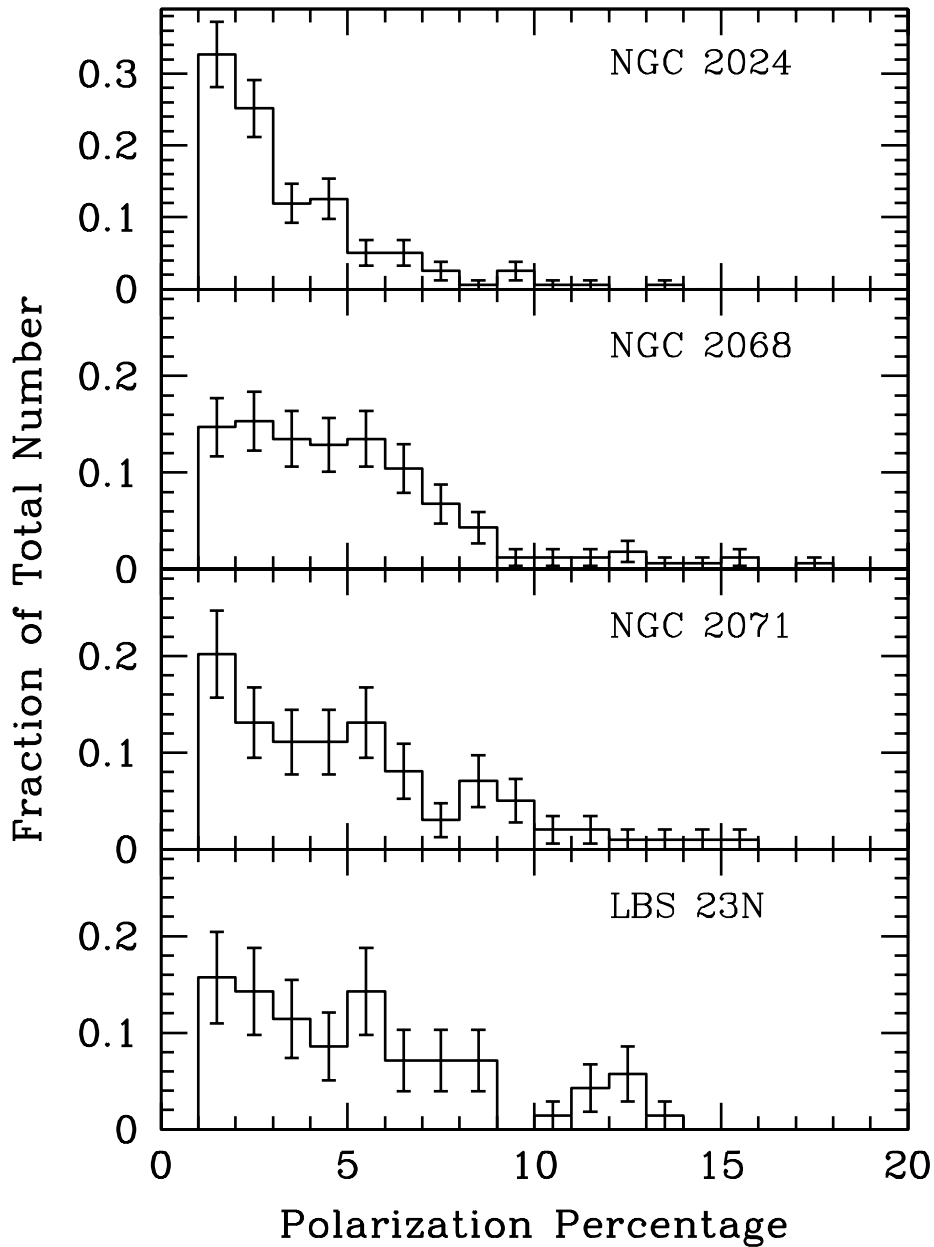


Fig. 5.— The distribution of polarization percentage in four regions of Orion B. The distributions for NGC 2024, NGC 2071 and LBS 23N are from data presented in Paper III. Clearly, the distribution of NGC 2024 is most heavily weighted to small values of p . In contrast, the regions of NGC 2068 and LBS 23N, and, to a lesser extent, NGC 2071, all show a flat distribution out to $\sim 6\%$, where they then decline.

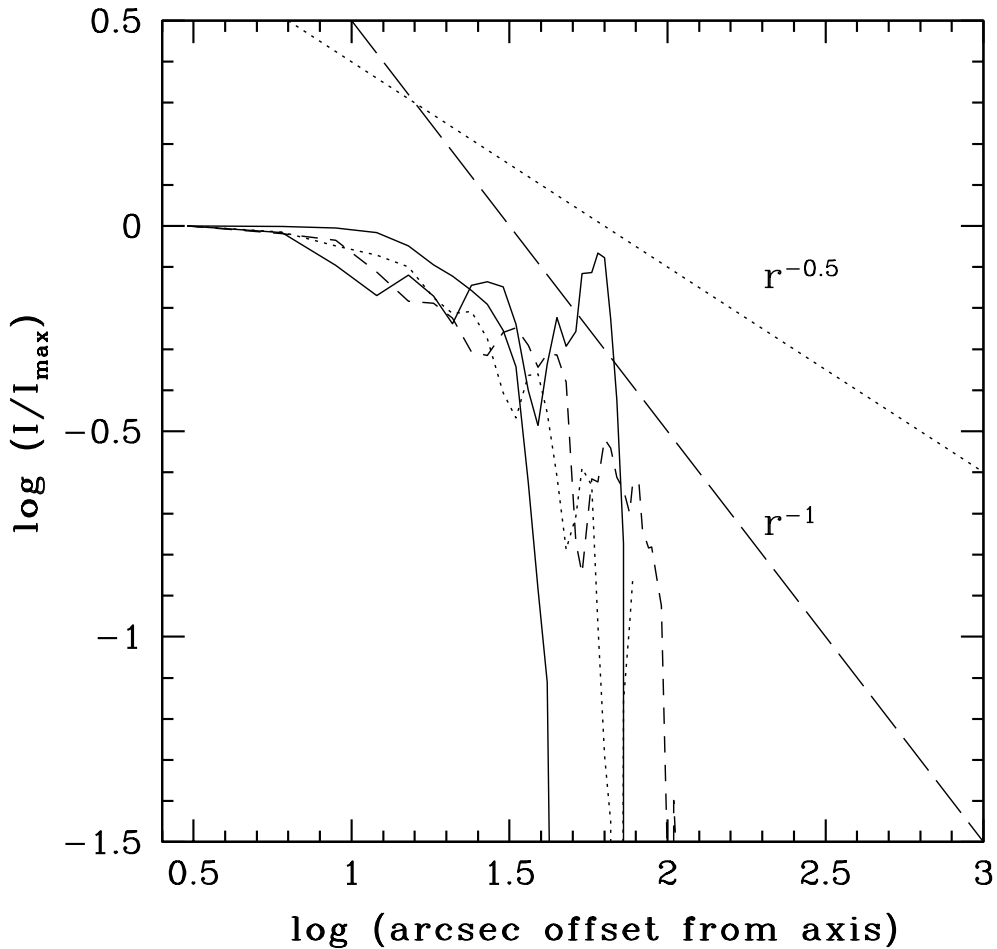


Fig. 6.— Radial flux profile of NGC 2068. A series of crosscuts shows the radial distribution of flux off the filament axis. The filament is very narrow so flux does not extend very far off the filament's axis (the intensity peak). Slices were taken between cores to avoid probing the profiles of very high density gas and dust. The positions of the cuts are discussed in the text. Assuming uncertainties of 10% in the intensities measurements, the uncertainty in each value of $\log(I/I_{\max})$ is ~ 0.08 . Slopes of r^{-1} and $r^{-0.5}$ flux profiles are shown.